# Modeling of magnetic-field-sensitive GaAs devices using 3D Monte Carlo simulation

C. Brisset [a,b], F.-X. Musalem [a], P. Dollfus [a], and P. Hesto [a]

[a] Institut d'Électronique Fondamentale, Bâtiment 220
Université Paris-Sud, 91405 Orsay cedex, France
[b] present adress: CEA, Service Électronique, BP 12
91680 Bruyères-le-Châtel, France

Abstract

The action of the Lorentz force on carrier motion is now included in MONACO, our 3D Monte Carlo device simulator. As examples we model two typical magnetic-field-sensitive devices, in which the detected signal is either the Hall voltage, or the induced current at two contacts. The results are in good agreement with expected characteristics.

## 1. Introduction

The trend towards the size reduction of integrated magnetic sensors makes necessary to account for geometrical effects and inhomogeneity of fields in theoretical prediction of galvanomagnetic phenomena governing device operation. Simulation tools are usually based on 2D numerical solution of macroscopic drift-diffusion equations augmented by magnetic-field-dependent terms [1]. Using the powerful Monte Carlo technique, studies of electron transport under homogeneous electric and magnetic fields [2] or in a gyrotron oscillator [3] have been also reported. This modeling technique can be applied to galvanomagnetic device simulation in order to gain insight into the description of physical phenomena involved in device operation. In this work, we present analyses of magnetic-field-sensitive devices using 3D Monte Carlo simulation.

## 2. The model

The main characteristics of MONACO, a 3D Monte Carlo device simulator, have been previously described [4,5]. The 3D Poisson equation is solved using a finite-elements scheme. The action of the Lorentz force on the carrier motion is now implemented in this software. This implementation is restricted to the case of spherical band structure leading to quite tractable equation of carrier motion. The magnetic field is uniformly applied in the device.

An important aspect of the algorithm used for the calculation of carrier trajectories is the detection of cell changes that allows to update in "real time" the electric field experienced by particles. This detection requires, before each free-flight, the calculation of the flight-time needed to reach a cell boundary, *i.e.*, the inversion of $\vec{r}(t)$ function. In this order,

the carrier real-space motion is simplified in the following manner. First the conductivity mass is assumed to be constant during the free flight and calculated as a function of the non parabolicity coefficient and the initial energy. This is all the more justified that duration of free-flight is smaller, *i.e.*, the energy change is lower. Second, by denoting $\omega_c$ the cyclotron frequency, the functions $\sin(\omega_c t)$ and $\cos(\omega_c t)$ are expanded in series terminated with the $(\omega_c t)^3$-term, which is perfectly justified for usual values of magnetic field and mean free time between collisions. This yields a third degree power function $\vec{r}(t)$ from which the flight-time needed to reach a cell boundary is easily extractable. However, by using this simplified approach, the energy gained by the particle in real space may be slightly inconsistent with its motion in $\vec{k}$-space. To ensure consistency, the final components of wave vector are adjusted *a posteriori* without significant error.

## 3. Simulation of magnetic sensors

We have simulated the two structures schematized in Fig.1, consisting of a uniformly doped GaAs bar ($N_D=10^{16}cm^{-3}$) with two electrodes (DEV-a) and four electrodes (DEV-b). In both devices the length L separating the bias electrodes numbered 1 and 2 is 3μm, the width W is 6μm, and the contact width $W_c$ is 2μm. DEV-b differs from DEV-a by the presence of two lateral electrodes numbered 3 and 4.

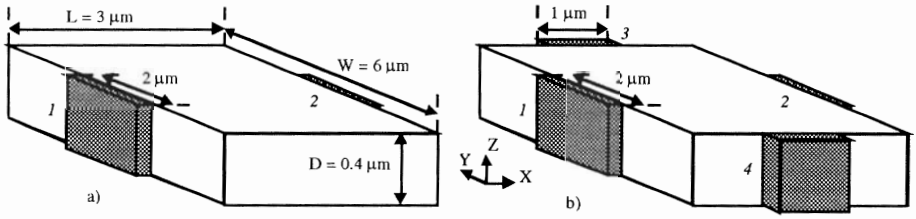


Figure 1: Simulated stuctures (GaAs, $N_D=10^{16}cm^{-3}$) ; a) DEV-a ; b) DEV-b

In both devices a voltage $V_X$= 0.3V is applied between the contacts numbered 2 and 1 to set the electric field $E_X$ about 1kV/cm. A vertical magnetic field $B_Z$ is uniformly applied in the whole structure. In DEV-a, it results in the building of an electric field $E_Y$ and then of a Hall voltage $V_H$ across the device width. In DEV-b the contacts 3 and 4 are short-circuited and the combination of electric field $E_X$ and magnetic field $B_Z$ induces a current $I_H$ between these contacts.

Fig.2 illustrates the equipotential lines in a XY-plane resulting from an applied magnetic field $B_Z$ = 0.8 T in DEV-a and Fig.3 shows the potential profiles along the width of the structure for several X positions. Under these field conditions the Hall voltage developed across the device is $V_H$ = 95 mV. Fig.4 is a plot of $V_H$ as a function of applied $B_Z$. For $B_Z \leq 0.6$ T the linearity of $V_H(B_Z)$ is excellent (S = 127 mV/T), in agreement with the usual expression of Hall field $E_Y$:

$$E_Y = -\omega_c \frac{\langle \tau_m^2 \rangle}{\langle \tau_m \rangle} E_X = -\frac{q}{m^*} \frac{\langle \tau_m^2 \rangle}{\langle \tau_m \rangle} E_X B_Z \qquad (1)$$

By defining the Hall mobility as $\mu_H = R_H \sigma = V_H / E_X B W_c$, the obtained value of 6350 $cm^2/Vs$ is in good agreement with experimental ones.

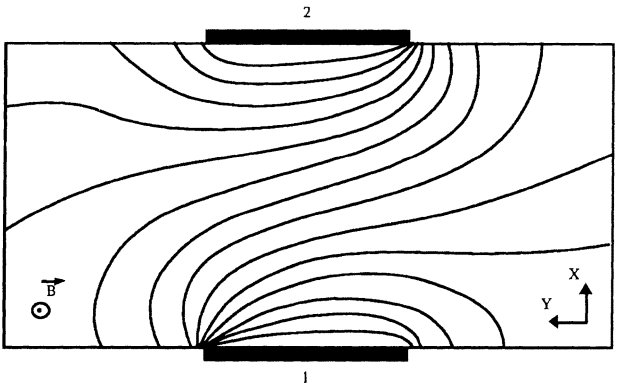


Figure 2: Equipotential lines in DEV-a.($V_X$=0.3V, $B_Z$=0.8T)

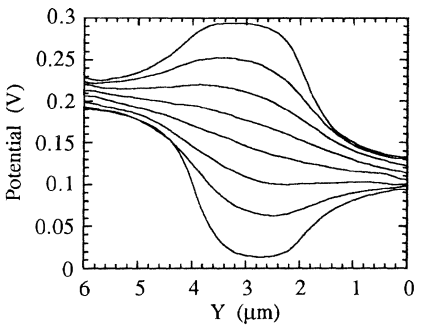


Figure 3: potential profiles along width in DEV-a for different X values. ($V_X$=0.3V, $B_Z$=0.8T).

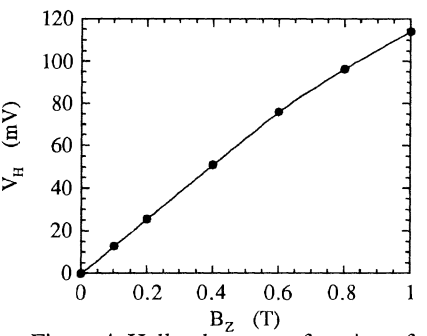


Figure 4: Hall voltage as a function of magnetic field in DEV-a. ($V_X$=0.3V).

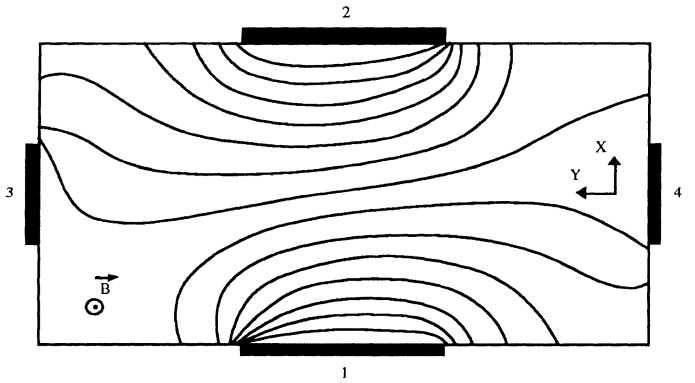


Figure 5: Equipotential lines in DEV-b.($V_X$=0.3V, $B_Z$=0.8T)

Fig.5 shows the equipotential lines in a XY-plane of DEV-b for $B_Z = 0.8$ T, with electrode 3 and 4 short-circuited. The magnetic field-induced-current $I_Y = I_H$ is plotted as a function of $B_Z$ in Fig.6. This plot is very well fitted (solid line in Fig.6) by a function similar to the theoretical expression of the current density $j_Y$ given by:

$$j_Y = \frac{n\,q^3}{m^{*2}} \left\langle \tau_m^2 \right\rangle E_X \frac{B_Z}{1 + \frac{q^2 \left\langle \tau_m^2 \right\rangle}{m^{*2}} B_Z^2} \tag{2}$$

The best fit is obtained for $\left\langle \tau_m^2 \right\rangle = 3.9 \times 10^{-26}$ s. Introducing this value in eq. (1) yields a scattering factor $r_H = \left\langle \tau_m^2 \right\rangle / \left\langle \tau_m \right\rangle^2$ about 1.3.

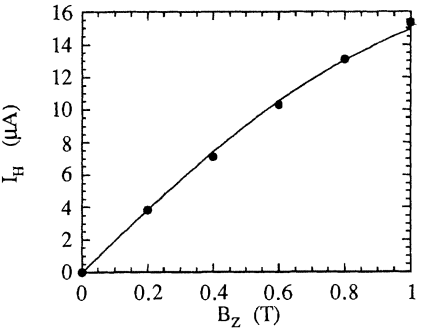


Figure 6: lateral current as a function of magnetic field in DEV-b. ($V_X$=0.3V).

## 4. Conclusion

MONACO is now a powerful 3D simulation tool for investigation of magnetic sensors and devices (magnetotransistors, Hall structures,...). Qualitative and quantitative results on typical magnetic-field-sensitive devices shown in this work validates our approach. Complex geometries including heterostructures may be now taken into account.

## References

[1] C. Riccobene, G. Wachutka, J. Bürgler, H. Baltes, *IEEE Trans. Electron Devices*, vol. ED 41, pp. 32-43, 1994

[2] D. Chattopadhyay, *J. Appl. Phys.*, vol. 45, pp. 4931-4933, 1974

[3] A.K. Ganguly, B.H. Hui, K.R. Chu, *IEEE Trans. Electron Devices*, vol. ED 29, pp. 1197-1209, 1982

[4] C. Brisset, P.Dollfus, N.Chemarin, R.Castagné, P.Hesto, Proc. SISDEP'93, pp. 189-192, 1993

[5] C.Brisset, P.Dollfus, O.Musseau, J.-L.Leray, P.Hesto, IEEE Trans. Nucl. Sci. vol. 41, pp. 2297-2303, 1994

# Quasi Three-Dimensional Simulation of Heat Transport in Thermal-Based Microsensors

A. Nathan[a] and N.R. Swart[b]

[a]Electrical and Computer Engineering, University of Waterloo
Waterloo, Ontario N2L 3G1, Canada
on leave at: Physical Electronics Laboratory, ETH Hoenggerberg
CH-8093 Zurich, Switzerland
[b]Institut National d'Optique, Sainte-Foy, Quebec G1P 4N8, Canada

Abstract

Results based on quasi three-dimensional numerical solutions of electrothermal behaviour in thermally isolated microstructures are presented. Here, we solved the two-dimensional system of electrothermal equations with heat loss to the surrounding (due to natural convection) incorporated as a mixed boundary condition. The convective heat loss was calculated based on a three-dimensional solution to the heat conduction equation using a boundary element method. The technique, employed in the analysis of heat transfer in a μ-Pirani gauge, yields numerical soultions which provide good agreement with measurement data.

## 1. Introduction

Thermal-based microsensors are required in a variety of sensing applications including detection of flow rate [1], pressure (vacuum) [2], and gas species [3]. In flow sensing, the heat loss from a resistively heated microstructure (due to forced convection) is modulated by the flow rate. In gas sensing, an isothermal heat surface (microhotplate) can be used to raise the temperature of the sensing film to increase absorption or reaction of gas on the film surface. With pressure sensing (based on the Pirani principle), heat transfer from a heating element is modulated by the mean free scattering length of molecules (or gas thermal conductance) which is pressure-dependent.

For insight into device operation including underlying heat transport mechanisms and for optimization of device design to meet key requirements of fast response time, low operating power and temperature, fast thermal response, it is necessary to solve the coupled system of equations governing electrothermal behaviour. Of particular importance in all of the above applications, is the modeling of heat loss from the microstructure to the ambient. For example, with the microstructure we have considered here (see Figs. 1 and 2), the heat loss due to natural convection can be as much as 99% of the input power at standard temperature and pressure (STP) [4]. Thus accurate modeling of the boundary condition accounting for the convective heat loss is crucial in a two-dimensional simulation.

## 2. Assumptions, Model Equations, and Numerical Procedure

In view of the planar nature of thermally isolated microstructures and because of small film thicknesses (relative to other linear dimensions), the electrothermal behaviour within the structure can be adequately described in two-dimensions. The approximation, although reasonable in terms of electrical behaviour, may not be intuitively obvious from a thermal standpoint and requires justification. In most structures, under conditions of natural convection in the diffusive limit (i.e. stagnant fluids), the Biot number is relatively small; this number describes the ratio of the surface heat conductance to the internal heat conductance across the microstructure thickness. Measurements performed on heat transfer test structures show that the gradient across the thickness at STP is negligible compared to the lateral gradients [5]. Given these conditions, electrical and heat transport within the microstructure can be described by the following 2-D system:

$$\nabla_{x,y} \cdot [\sigma(T)\, \nabla_{x,y}\, \psi] = 0 \tag{1}$$

$$\nabla_{x,y} \cdot [\kappa(T)\, \text{grad}\, T] = \sigma(T)\, (\nabla_{x,y}\, \psi)^2. \tag{2}$$

Here, $\sigma(T)$ denotes the temperature-dependent electrical conductivity of the polysilicon regions (see Fig. 2), $\psi$ is the electric potential, $\kappa(T)$ is the temperature-dependent thermal conductivity, and T is the temperature. The term on the right-hand-side of eqn. (2) denotes Joule heat.

In the presence of a flow stream, the steady-state heat transport from the surface of the microstructure, assuming negligible viscous dissipation, is governed by the energy equation:

$$\rho C_p\, [u\, \partial T/\partial x + v\, \partial T/\partial y + w\, \partial T/\partial z] = \nabla \cdot (\kappa(T)\, \nabla\, T) \tag{3}$$

where u, v, and w are the components of the velocity field, $\rho$ is the density, and $C_p$ is the specific heat. With zero flow, we can assume that the natural convective currents are negligible. Despite the excessively high ($\approx$ 400 °C) in-situ heated temperatures, the resulting Grashof number, which describes the ratio of buoyancy to viscous fluid forces, is small. Measurements show that the heat loss from such microstructures is independent of its orientation with respect to the gravity vector [5]. Thus we can assume that the fluid is stagnant (diffusive) and that the temperature distribution obeys $\nabla \cdot (\kappa(T)\, \nabla\, T) = 0$ where $\kappa(T)$ denotes the thermal conductivity of the fluid expanse (air) and is pressure-dependent. For given surface temperature of the microstructure, $T_s(x,y)$, the temperature of the micromachined cavity walls, and the temperature of the fluid far from the microstructure surface (free stream temperature, $T_\infty$), the equation can be solved to determine the convective heat loss from the microstructure surface to the surrounding [5]. This heat loss constitutes the boundary condition required for eqn. (2). The technique to solve this equation is based on a boundary element method along the lines reported in [6]. However, it can be reduced to Laplace's equation by employing Kirchoff transformation and this intrinsically accounts for the

temperature dependence of the thermal conductivity [7]. Based on the solution, we calculate a heat transfer function $G(x,y)/(\kappa°C)$ on the membrane surface. The surface heat density at position (x,y) on the membrane surface

$$q_s = \kappa\, G(x,y)\, [T_s(x,y) - T_\infty] \tag{4}$$

is then employed as a mixed boundary condition for the two-dimensional solution of eqn. (2). Since the heat transfer function G(x,y) is a function of $T_s(x,y)$, it is recalculated within the iterative loop used in the solution of eqns. (1) and (2). Radiative heat losses, if necessary, can also be incorporated as a mixed boundary condition. In our case, in view of the given device active area and input powers involved, such losses are negligible.

Equations (1) and (2) are discretized using a control area approximation with node count of 1600 and 4700, respectively, for the structure shown in Fig. 1. The procedure starts with the calculation of G(x,y), following which a system of equations for the electrical conduction equation is generated. Based on the solution, the Joule heat terms are calculated and eqn. (2) is solved. Since (2) can be potentially nonlinear, an inner iterative loop is employed. The solution of the systems of equations is based on a conjugate gradient scheme. Solution verification is based on electrical and heat flux conservation checks.

## 3. Results and Discussion

The simulated temperature distribution in the device (see Figs. 1and 2) in air at STP is illustrated in Fig. 3. The peaks and valleys correspond to the temperature distribution of the active (current carrying) and passive (temperature sensing) coils, respectively. The thermal behaviour of both coils was measured for both air and helium at STP. The temperature values shown were based on measurements of coil resistance from which an average coil temperature is retrieved following prior temperature coefficient characterization of the polysilicon layer. The temperature difference between active ($T_{ac}$) and passive coils is illustrated in Fig. 4 as a function of the input power. With maintaining the active coil average temperature at 70°C, we clearly see that the input power (heat loss) is consistent with the thermal conductivities of the two gases implying an almost 100% transduction efficiency. The larger temperature difference in the case of helium is due to the convective heat loss to the surrounding which predominates over the inter-coil lateral heat transfer.

## 4. Conclusions

In this paper, we have presented the necessary assumptions, resulting model equations, and boundary conditions pertinent to two-dimensional numerical simulation of heat transport in thermal-based microsensors taking into account convective heat losses. The simulations provide good agreement with measurement data.

## References


[1] R.G. Johnson and R.E. Higashi, Sensors and Actuators, vol. 11 (1987) 63.
[2] A.W. van Herwaarden and P.M. Sarro, J. Vac. Sci. Tech., vol. A5 (1987) 2454.
[3] J.S. Suehle, R.E. Cavicchi, M. Gaitan, and S. Semancik, IEEE Electron Dev. Letts., vol. 14 (1993) 118.
[4] N.R. Swart and A. Nathan, Tech. Digest, IEEE IEDM, 1994, p. 135.
[5] N.R. Swart, Heat Transport in Thermal-Based Microsensors, Ph.D. dissertation, University of Waterloo, 1994.
[6] K. Nabors and J. White, IEEE Trans. CAD, vol. 10 (1991) 1447.
[7] W. Allegretto, B. Shen, Z. Lai, and A.M. Robinson, Sensors and Materials, vol. 6 (1994) 71.


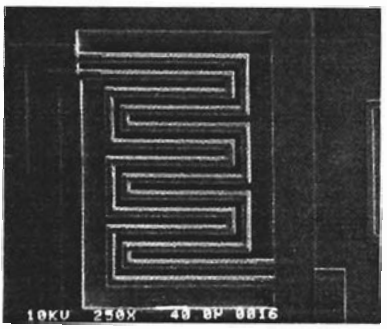


**Fig. 1** Photomicrograph of device used in simulations.

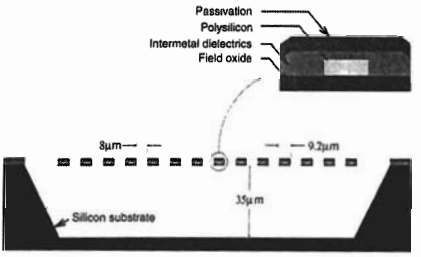


**Fig. 2** Device cross-section.

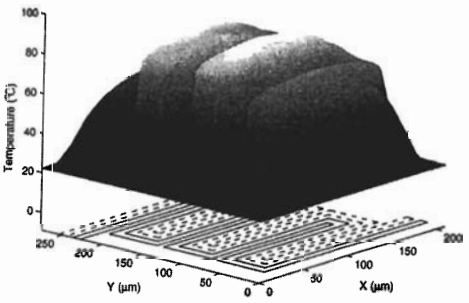


**Fig. 3** Temperature distribution in device at STP (dashed line: active coil, solid line: passive coil).

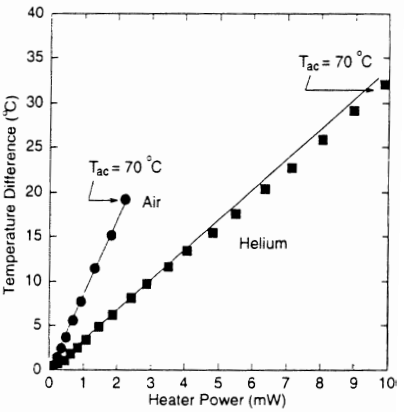


**Fig. 4** Temperature difference between coils as a function of input power (solid lines: simulations, points: measured values)